Title
Persistence behavior of heat and momentum fluxes in convective surface layer turbulence

Journal
Physics of Fluids, 32(11)

ISSN
1070-6631

Authors
Chowdhuri, Subharthi
Prabhakaran, Thara
Banerjee, Tirtha

Publication Date
2020-11-01

DOI
10.1063/5.0027168

Peer reviewed

Physics of Fluids

Persistence behavior of heat and momentum fluxes in convective surface layer turbulence

Cite as: Phys. Fluids 32, 115107 (2020); https://doi.org/10.1063/5.0027168
Submitted: 28 August 2020 . Accepted: 16 October 2020 . Published Online: 04 November 2020

Subharthi Chowdhuri, Thara Prabhakaran, and Tirtha Banerjee

Physics of Fluids ARTICLE scitation.org/journal/phf

Persistence behavior of heat and momentum fluxes in convective surface layer turbulence

Cite as: Phys. Fluids 32, 115107 (2020); doi: 10.1063/5.0027168
Submitted: 28 August 2020 • Accepted: 16 October 2020 •
Published Online: 4 November 2020

Subharthi Chowdhuri,[1,a)] Thara Prabhakaran,[1] and Tirtha Banerjee[2]

AFFILIATIONS

[1] Indian Institute of Tropical Meteorology, Ministry of Earth Sciences, Dr. Homi Bhaba Road, Pashan, Pune 411008, India
[2] Department of Civil and Environmental Engineering, University of California, Irvine, California 92697, USA

[a)] Author to whom correspondence should be addressed: subharthi.cat@tropmet.res.in

ABSTRACT

The characterization of heat and momentum fluxes in wall-bounded turbulence is of paramount importance for a plethora of applications ranging from engineering to Earth sciences. Nevertheless, how the turbulent structures associated with velocity and temperature fluctuations interact to produce the emergent flux signatures has not been evident until now. In this work, we investigate this fundamental issue by studying the switching patterns of intermittently occurring turbulent fluctuations from one state to another, a phenomenon called persistence. We discover that the persistence patterns for heat and momentum fluxes are widely different. Moreover, we uncover power-law scaling and length scales of turbulent motions that cause this behavior. Furthermore, by separating the phases and amplitudes of flux events, we explain the origin and differences between heat and momentum transfer efficiencies in convective turbulence. Our findings provide a new understanding of the connection between flow organization and flux generation mechanisms, two cornerstones of turbulence research.

I. INTRODUCTION

The ensemble averaged vertical turbulent fluxes of momentum or heat are expressed as the covariance between the vertical and streamwise velocity fluctuations ($\overline{u'w'}$) or between the vertical velocity and temperature fluctuations ($\overline{w'T'}$). The primes in the flux expressions denote the turbulent fluctuations in the streamwise velocity (u'), vertical velocity (w'), or temperature (T'). The overline symbol indicates the average over several ensemble members. For practical purposes, such an ensemble average is replaced by the average over time or space by applying the ergodic hypothesis.[1] In turbulent flows, these fluxes quantify the amount of heat or momentum being transported from (to) the surface to (from) other locations. The sign convention dictates that the positive or negative values of the fluxes denote the direction of the transport from or toward the surface. The estimation of these fluxes has numerous uses, such as in wall-bounded turbulent flows, the momentum transport toward the wall is related to surface drag, which determines the power requirements and efficiencies in many engineering applications.[2,3] Additionally, in the geophysical context, these fluxes quantify the surface-atmosphere momentum and heat exchanges, which eventually drive the Earth's climate.[4,5] Therefore, it is of paramount importance to develop a comprehensive understanding of the turbulent generation mechanisms of the heat and momentum fluxes. Since the flux computation involves the product of two turbulent quantities, a fundamental research question is *how do the turbulent structures (of different time or length scales) associated with the velocity and temperature fluctuations interact to produce the momentum and heat flux signatures*?

The common method of describing the fluctuation characteristics and the associated fluxes, corresponding to the different scales of the turbulent motions, is the spectral approach.[6] However, a landmark study by Kline *et al.*[7] noted that the transport of momentum in wall-bounded shear flows was not a continuous process, as assumed by the spectral analysis. Instead, they found that the intermittent ejections of low-momentum fluid parcels from the wall ($u' < 0$ and $w' > 0$) accompanied with the sweeps of high-momentum fluid toward the wall ($u' > 0$ and $w' < 0$) were responsible for the generation of the momentum flux. Subsequently, to diagnose the intermittent signatures of the ejection and sweep motions and estimate their contributions toward the momentum flux, a conditional sampling technique named quadrant analysis was introduced.[8–10] In addition to quadrant analysis, a few studies also noted that the ejection and sweep motions in wall-bounded turbulent flows occurred with a range of different time scales as more often than not they switched irregularly from one quadrant state to the other.[11–13] While evaluating the statistical characteristics of these time scales, Rao, Narasimha, and Badri Narayanan[11] and Alfredsson and Johansson[12] found that the mean time scales of the burst events (sequence of ejections exceeding a certain threshold) in the near-wall region were influenced by both the small and large scale motions.

Such results were intriguing, considering their relevance to the connection between the turbulent structures of different time scales and the intermittent generation of the momentum fluxes. Nevertheless, a detailed treatment of the time scale distribution of the flux-carrying motions was severely lacking.[14] To tackle this problem, Kailasnath and Sreenivasan[15] demonstrated that the probability density functions (PDFs) of the time scales of the turbulent motions contributing to the momentum flux can be systematically studied by exploring the zero-crossing properties of the instantaneous $u'w'$ signal. Their method was inspired by the results of Sreenivasan, Prabhu, and Narasimha[16] where the PDFs of the time intervals between the zero-crossings of the turbulent fluctuations were used to probe the distribution of time scales in a wall-bounded flow. In the parlance of non-equilibrium statistical mechanics, the distribution of zero-crossing time intervals in a stochastic signal is equivalent to the persistence PDFs, where persistence is the probability $P(t)$ that the signal does not change its sign up to the time t.[17–19] Hereafter, we refer to the zero-crossing PDFs as the persistence PDFs, given its technical suitability.[19]

One of the crucial aspects of the study by Kailasnath and Sreenivasan[15] was to investigate how the persistence PDFs of the individual velocity signals compared to the persistence PDFs of their product, which constituted the momentum flux. They found that in the inertial layer of a flat-plate boundary layer, the persistence PDFs of the momentum flux signal closely followed the same PDFs of the vertical velocity fluctuations, with both displaying a nearly identical single exponential function. This was in sharp contrast with the streamwise velocity fluctuations, whose persistence PDFs displayed a double exponential structure with two different exponents. They interpreted this behavior as both the small and large scales were relevant for the variations in the streamwise velocity fluctuations. However, for the variations in the wall-normal velocity and the momentum flux, only the large scales were primarily responsible, since their zero-crossing PDFs displayed a single exponential function. Moreover, they also proposed a connection to associate such behavior with the properties of the attached eddies, which populated the inertial layer, consistent with the Townsend's attached eddy hypothesis.[20]

In general, the findings of Kailasnath and Sreenivasan[15] shed light on the fundamental issue of the relationship between the turbulent structures of different scales and the associated intermittent flux signatures. However, while evaluating the time scales of the momentum flux signals, they did not consider the quadrant effects. We hypothesize that the conditional sampling of the flux events can establish an important link between the momentum flux partition among the four different quadrants and the time scales of the turbulent flow. Such an analysis can identify the time scales associated with individual quadrant motions that contribute toward momentum flux generation. Lately, the concept of persistence has been used; (a) to estimate the integral length scale in wall-bounded turbulent flows,[21] (b) to compute the dissipation rate of turbulence kinetic energy in atmospheric, canopy, and laboratory flows,[22–25] or (c) to assess the non-Gaussian effects in canopy turbulence.[26] However, to the best of our knowledge, there has been no related studies to scrutinize the persistence characteristics of the turbulent fluxes and the associated quadrant effects. Although until now, we have discussed the features of the momentum flux signal in turbulent shear flows, it can be noted that even in buoyancy-driven turbulent flows, the instantaneous heat flux signals ($w'T'$) display similar intermittent signatures.[27,28] Therefore, such investigation will be pertinent for a convective atmospheric boundary layer (ABL) flow, where both shear and buoyancy play significant roles to maintain the turbulence. From a practical perspective, the measurements in an ABL flow are often conducted within the layer closer to the surface, known as the atmospheric surface layer (ASL).

The ASL is a generalization of the inertial layer of wall-bounded shear flows by including the effect of buoyancy.[29,30] The vertical extent of the ASL is approximately up to the lowest 10% of the convective boundary layer (excluding the roughness sublayer) where the fluxes are nearly constant with height.[31] During the early days of ASL research, Haugen, Kaimal, and Bradley[32] observed that in convective conditions, the time traces of the instantaneous $w'T'$ signals displayed intermittently occurring long sequences of positive heat flux events. They further noted that the time-averaged characteristics of the heat flux and their transport efficiencies (expressed through the correlation coefficient between w' and T') were primarily determined by these long persistent events. On the other hand, for the instantaneous $u'w'$ signals, the long sequences of the flux-carrying motions transported momentum either in the upward or in the downward direction. In a highly convective ASL flow (characterized by strong thermal stratification), the amplitudes of the large persistent positive and negative momentum flux events were almost similar to each other. This caused the time-averaged momentum flux to become quite small due to the near-perfect cancellation of such positive and negative values. However, with the decrease in the strength of the thermal stratification (near-neutral ASL), the negative amplitudes associated with the long sequences overwhelmed the positive ones. Therefore, the momentum transport efficiency increased as the ASL approached the near-neutral conditions. Haugen, Kaimal, and Bradley[32] postulated that such changes associated with thermal stratification were related to the changes in the topology of coherent structures from cellular patterns to horizontal rolls. Nevertheless, their conclusions were based on visual inspections of a few 15-min records and were of a qualitative nature.

Since then, numerous studies have documented that akin to laboratory flows, the heat and momentum transport processes in a convective ASL are intermittent in nature, which occur with a range of different time scales.[33–37] Additionally, several other researchers have demonstrated that the time-averaged transport characteristics of the heat and momentum in a convective ASL flow are strongly dependent on the strength of the thermal stratification.[38–40] Specifically, these studies show that in a highly convective ASL, the heat and momentum transports are decoupled from each other, whereas they are strongly coupled under near-neutral conditions. Recently, Salesky, Chamecki, and Bou-Zeid[41] have illustrated that, with unstable stratification, the change in the topology of the coherent structures in a convective flow influences the transport efficiencies of the heat and momentum.

Broadly, the characteristics of the time-averaged heat and momentum fluxes in a convective ASL flow could be perceived as a well-researched problem. However, since the times of Haugen, Kaimal, and Bradley,[32] a grand challenge still remains to connect the intermittent behavior of these fluxes with the different scales of the turbulent eddies, which influence their component signals. Recently, the statistical characteristics of eddy time scales for velocity and temperature fluctuations in convective ASL flows have been established by Cava *et al.*[42] and Chowdhuri, Kalmár-Nagy, and Banerjee[19] through persistence analysis. They have shown that at scales smaller than the integral scales, the PDFs of the persistence time scales follow a power-law behavior with a sharp exponential cutoff. However, these former studies did not consider the associated effect of such behavior on the products of the velocity and temperature signals, which constitute the turbulent fluxes. Undoubtedly, such investigation is timely and of fundamental interest to improve our understanding of the generation mechanisms of the heat and momentum fluxes. This problem also has practical implications regarding the development of next-generation transport models of convective turbulence. To address these issues, we ask the following questions:

1. What type of event signatures are generated in the momentum and heat flux signals due to the presence of turbulent eddies of different time scales?
2. What is the relation between these event signatures at different time scales with the heat and momentum transport efficiencies in a convective ASL flow?
3. How does the change in the thermal stratification modulate the event signatures at different time scales?

In this article, we attempt to answer these questions through persistence analysis of the turbulent heat and momentum fluxes in a convective ASL flow. We organize this paper as follows: In Sec. II, we provide brief descriptions of the field-experimental dataset and methodology, in Sec. III, we introduce the results and discuss them, and finally, in Sec. IV, we summarize the key takeaways and provide the scope for further research.

II. DATASET AND METHODOLOGY

In this study, we have used the dataset from the Surface Layer Turbulence and Environmental Science Test (SLTEST) experiment. The details about the SLTEST experiment and the setup of the instruments are provided in the works of Chowdhuri, Kumar, and Banerjee[43] and Chowdhuri, Kalmár-Nagy, and Banerjee.[19] In this experiment, nine north-facing time synchronized CSAT3 sonic anemometers were deployed on a 30-m mast, spaced logarithmically from 1.42 m to 25.7 m, with the sampling frequency being set at 20 Hz. We followed the same data processing steps as outlined in the work of Chowdhuri, Kalmár-Nagy, and Banerjee[19] to select the 30-min periods from the daytime convective conditions. Totally, 261 combinations of the stability ratios ($-\zeta = z/L$, where z is the measurement height and L is the Obukhov length) were possible for these selected 30-min periods. In an ASL flow, the Obukhov length (L) is defined as

$$L = -\frac{u_*^3 T_0}{k_v g H_0}, \tag{1}$$

where T_0 is the surface air temperature (K), g is the acceleration due to gravity (9.8 m s^{-2}), H_0 is the surface kinematic heat flux (m s^{-1} K), k_v is the von Kármán constant (0.4), and u_* is the friction velocity (m s^{-1}). Furthermore, the entire range of $-\zeta$ ($12 \le -\zeta \le 0.07$)

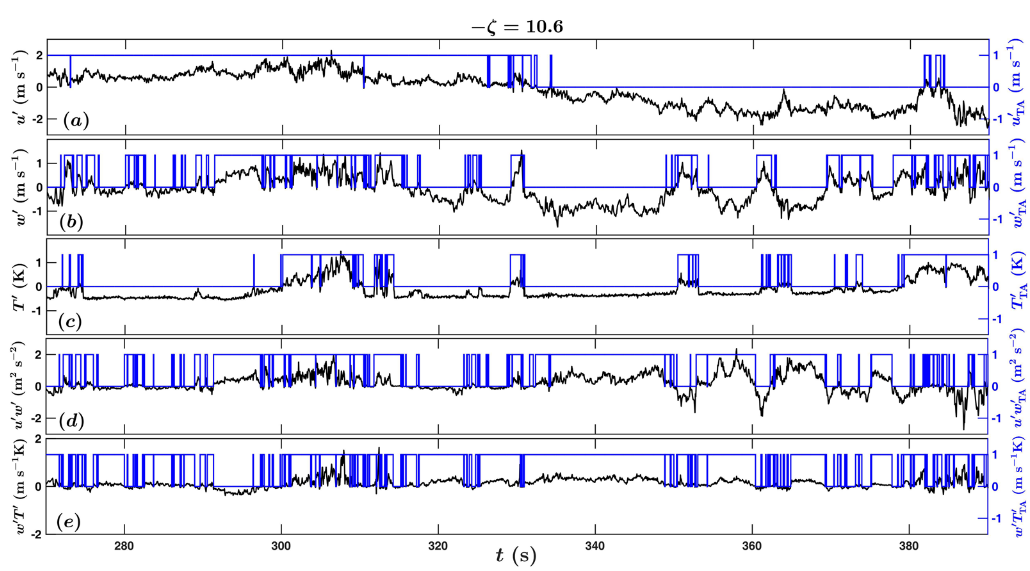

FIG. 1. A 120-s long section of a time series of (a) u', (b) w', (c) T', (d) $u'w'$, and (e) $w'T'$ from a highly convective surface layer corresponding to a $-\zeta = 10.6$ is shown. The actual values are displayed as black solid lines, which correspond to the left-hand side of the y axis. Similarly, the associated telegraphic approximations (TA) are displayed as blue solid lines, which correspond to the right-hand side of the y axis.

was divided into six stability classes and considered for the persistence analysis of the turbulent heat and momentum fluxes. These are the same set of stability classes used by Chowdhuri, Kumar, and Banerjee[43] and Chowdhuri, Kalmár-Nagy, and Banerjee[19] for their study of turbulence anisotropy and persistence behavior of turbulent velocity and temperature fluctuations (see their respective Tables 2 and 1). For the sake of brevity, the same information is not repeated here.

A graphical demonstration of the persistence phenomenon is provided in Fig. 1, where a 120-s long section of streamwise velocity fluctuations (u'), vertical velocity fluctuations (w'), temperature fluctuations (T'), and their products representing the instantaneous streamwise momentum ($u'w'$) and heat fluxes ($w'T'$) are shown for a particular 30-min run, corresponding to $-\zeta = 10.6$. The associated telegraphic approximations (TA) of these time series are presented at the right-hand side of the y axis in Fig. 1, displayed in blue [see Eq. (2)]. This representation helps identify the switching patterns in a time series where the TA values change from 0 to 1 or 1 to 0. A visual inspection of Fig. 1 suggests that the w' signals switch more often from the positive (negative) to the negative (positive) turbulent states as compared to the u' or the T' signals. However, the streamwise momentum ($u'w'$) and the heat flux ($w'T'$) signals involve both the combinations of the w' and u' or w' and T' signals. Therefore, the switching tendencies of these turbulent fluxes [Figs. 1(d) and 1(e)] must be related to the persistence signatures of their component signals. This issue is discussed further in Sec. III A.

As described by Chowdhuri, Kalmár-Nagy, and Banerjee,[19] the persistence time (t_p) is defined as the time up to which a fluctuating turbulent signal stays positive or negative before being switched to the other state. In addition to that, the associated probability density function (PDF) of t_p describes its statistical characteristics, which in turn are related to the turbulent structures in a convective flow.[19] We apply these same concepts in the present study to investigate the persistence behavior of the instantaneous heat and momentum flux signals. Typically, we encounter in the order of 10^5 number of zero-crossings for the u', w', T', $u'w'$, and $w'T'$ signals for every six stability classes.[19] Therefore, the persistence PDFs of the $u'w'$ and $w'T'$ signals for each of these six stability classes are constructed over these large number of ensemble events to ensure their statistical robustness. Note that the persistence PDFs are computed via logarithmic binning and subsequent transformation to the linear space using a change of variable, as illustrated by Chowdhuri, Kalmár-Nagy, and Banerjee.[19] In Sec. III, we discuss the properties of the persistence PDFs of the streamwise momentum and the heat flux signals corresponding to these six stability classes.

III. RESULTS AND DISCUSSION

We begin by presenting the results of the persistence PDFs of the instantaneous momentum and heat flux signals ($u'w'$ and $w'T'$), including a comparison with the persistence of the component signals themselves (u', w', and T'). Subsequently, we discuss the effect of separation into four different quadrants on the persistence PDFs of the flux signals. Furthermore, we explore the role of the intermittent flux events of different persistence time scales toward the heat and momentum transport efficiencies. In order to achieve such objectives, we introduce a novel approach to separate the phases and amplitudes of the component signals associated with such events of various time scales. Additionally, we also provide plausible physical explanations of the obtained results during the course of our presentation.

A. Persistence PDFs of heat and momentum fluxes

Prior to embarking on a detailed analysis regarding the persistence PDFs of the heat and momentum flux signals, perhaps it is prudent to establish a phenomenological connection between the persistence properties of the fluxes and their component signals. In order to derive such relation, we turn our attention toward the telegraphic approximations (TA) of the turbulent signals. Specifically, we ask the question *if the TA representation of the component signals is known, then what would be the equivalent TA representation of their product*?

1. Association between the persistence time scales of the flux and its components

The TA representation of any turbulent signal s' can be expressed as[42,44]

$$(s')_{\mathrm{TA}} = \frac{1}{2}\left(\frac{s'(t)}{|s'(t)|} + 1\right). \tag{2}$$

Now, if we have a product of two signals x' and w' (where x can be either u or T), then from Eq. (2), the TA representation of $x'w'$ can be written as

$$(x'w')_{\mathrm{TA}} = \frac{1}{2}\left(\frac{x'w'(t)}{|x'w'(t)|} + 1\right). \tag{3}$$

By using an identity $|AB| = |A| \times |B|$, we can further rewrite Eq. (3) as

$$(x'w')_{\mathrm{TA}} = \frac{1}{2}\left(\frac{x'(t)}{|x'(t)|} \times \frac{w'(t)}{|w'(t)|} + 1\right). \tag{4}$$

From Eq. (2), we know that

$$\frac{x'(t)}{|x'(t)|} = 2x'_{\mathrm{TA}} - 1, \tag{5}$$

$$\frac{w'(t)}{|w'(t)|} = 2w'_{\mathrm{TA}} - 1. \tag{6}$$

By substituting these in Eq. (4), we find that

$$(x'w')_{\mathrm{TA}} = \frac{1}{2}\left[\left(2x'_{\mathrm{TA}} - 1\right) \times \left(2w'_{\mathrm{TA}} - 1\right) + 1\right]. \tag{7}$$

By expanding Eq. (7) and after some algebraic manipulation, we get

$$(x'w')_{\mathrm{TA}} = 1 - [x'_{\mathrm{TA}}(1 - w'_{\mathrm{TA}}) + w'_{\mathrm{TA}}(1 - x'_{\mathrm{TA}})]. \tag{8}$$

Note that the variables x'_{TA} and w'_{TA} can take only two values, which are either 0 or 1. If we evaluate $[x'_{\mathrm{TA}}(1 - w'_{\mathrm{TA}}) + w'_{\mathrm{TA}}(1 - x'_{\mathrm{TA}})]$ at $w'_{\mathrm{TA}} = 1$, $x'_{\mathrm{TA}} = 1$, and $w'_{\mathrm{TA}} = 0$, $x'_{\mathrm{TA}} = 0$, we obtain

$$[x'_{\rm TA}(1-w'_{\rm TA})+w'_{\rm TA}(1-x'_{\rm TA})]=w'_{\rm TA}-x'_{\rm TA},(w'_{\rm TA}=1,x'_{\rm TA}=0,1), \quad (9)$$

$$[x'_{\rm TA}(1-w'_{\rm TA})+w'_{\rm TA}(1-x'_{\rm TA})]=x'_{\rm TA}-w'_{\rm TA},(x'_{\rm TA}=1,w'_{\rm TA}=0,1), \quad (10)$$

$$[x'_{\rm TA}(1-w'_{\rm TA})+w'_{\rm TA}(1-x'_{\rm TA})]=0,(x'_{\rm TA}=0,w'_{\rm TA}=0), \quad (11)$$

respectively. Equations (9)–(11) take into account all the four possible combinations of $x'_{\rm TA}$ and $w'_{\rm TA}$ values, such as {0, 0}, {0, 1}, {1, 0}, and {1, 1}. Apparently, we can condense these three expressions as

$$[x'_{\rm TA}(1-w'_{\rm TA})+w'_{\rm TA}(1-x'_{\rm TA})]=|x'_{\rm TA}-w'_{\rm TA}|. \quad (12)$$

By substituting Eq. (12) in Eq. (8), we get the final formula

$$(x'w')_{\rm TA}=1-|x'_{\rm TA}-w'_{\rm TA}|, \quad (13)$$

which connects the TA representation of the product with the TA's of the component signals. Some further discussion about comparing the prediction from Eq. (13) with the observation can be found in the Appendix.

From the definition of persistence, t_p is the time up to which $ds'_{\rm TA}/dt=0$ such that $s'_{\rm TA}$ remains in a particular state before switching to the other. Therefore, to connect the persistence time scales of the component signals with their product, we can differentiate Eq. (13) as

$$\frac{d}{dt}(x'w')_{\rm TA}=-\frac{d}{dt}|x'_{\rm TA}-w'_{\rm TA}|. \quad (14)$$

For the ease of calculation, we take a difference form of Eq. (14), expressed as

$$(x'w')_{\rm TA}(i+1)-(x'w')_{\rm TA}(i) = |x'_{\rm TA}(i)-w'_{\rm TA}(i)|-|x'_{\rm TA}(i+1)-w'_{\rm TA}(i+1)|, \quad (15)$$

where i is the time index. By rearranging the terms and considering the absolute magnitudes of the differences (switching between 0 and 1 or 1 and 0 is counted as same), Eq. (15) can be rewritten as

$$|\Delta(x'w')_{\rm TA}|=\left||\Delta x'_{\rm TA}|-|\Delta w'_{\rm TA}|\right|, \quad (16)$$

where for any signal $s'_{\rm TA}$, $\Delta s'_{\rm TA}=s'_{\rm TA}(i+1)-s'_{\rm TA}(i)$.

From Eq. (16), one can infer that the zero-crossings of $(x'w')_{\rm TA}$ will be located at those points where $|\Delta x'_{\rm TA}|\neq|\Delta w'_{\rm TA}|$. As a consequence, the persistence time scales of $x'w'$ will be related to the persistence time of that component signal, which switches its states more rapidly than the other one. We can anticipate that the persistence PDFs of the products of the turbulent signals will be closer to the persistence PDFs of the individual signals at small time scales. The reason is that the probability of occurrence of the events persisting for short times will not be much different for the x', w', and $x'w'$ signals, since all of them rapidly fluctuate. On the other hand, at large time scales, the persistence PDFs of the products are expected to be more closer to that signal, which has a lower chance of encountering such long sequences. Next, we describe how the insights gained from the aforementioned analysis compare with the observations of the persistence PDFs of heat and momentum fluxes in a convective ASL flow.

2. Features of the flux persistence PDFs

Figure 2 shows the persistence PDFs of the instantaneous streamwise momentum ($u'w'$) and heat fluxes ($w'T'$) compared with their component signals (u' and w' or w' and T') for the six stability classes in a convective ASL flow. In Fig. 2, the persistence time scales are converted to streamwise lengths ($t_p\overline{u}$, where $\overline{u}$ is the mean wind speed) by applying the Taylor's frozen turbulence hypothesis and scaled with z. Such scaling stems from the supposition that the eddies near the surface linearly grow with z.[30,45] Hereafter, we denote the converted streamwise lengths related to persistence as ℓ_p. Apart from that, the colored dashed arrows in Fig. 2 indicate the normalized integral length scales of u' (Λ_u/z, red dashed arrows), w' (Λ_w/z, blue dashed arrows), and T' signals (Λ_T/z, pink dashed arrows) computed from the exponential fits to the respective auto-correlation functions[19] (see Fig. 5 of their work for the auto-correlation plots).

One can notice from Fig. 2 that, irrespective of the stability classes, for length scales smaller than the integral scale of w' ($\ell_p\leq\Lambda_w$), the persistence PDFs of momentum or heat nearly collapse on the persistence PDFs of the individual component signals, such as u' and w' or T' and w'. However, for $\ell_p>\Lambda_w$, the persistence PDFs of the turbulent fluxes more closely follow the PDFs associated with the w' signal. The reason behind this observed phenomenon is twofold and in accord with the inferences drawn from Eq. (16). First, the integral scales of the u' and T' signals remain significantly larger than the w' signal. Second, Chowdhuri, Kalmár-Nagy, and Banerjee[19] have demonstrated that the persistence PDFs follow a power-law distribution up to the scales comparable with the integral scale before they start to drop off exponentially. Combining these two rationales, it is imperative that at larger time scales, greater than Λ_w, the persistence PDFs of w' would fall off faster than the u' or T' signals, given $\Lambda_w<\Lambda_{u,T}$. As a consequence, the flux persistence PDFs of $u'w'$ and $w'T'$ follow the same PDFs of the w' signals at scales larger than Λ_w while nearly matching with both the individual signals for the scales $\ell_p\leq\Lambda_w$.

To further explore the flux persistence PDFs, we note that the turbulent transports of heat and momentum are accomplished through events from four different quadrants, namely, the down-gradient and counter-gradient quadrants.[10] In a convective ASL, the transport efficiencies of the heat and momentum are intimately related to how the total fluxes are partitioned between the down-gradient and counter-gradient quadrants.[39] Therefore, as a first step to connect the persistence behavior of the fluxes at different scales with their transport characteristics, it is important to decompose the heat and momentum flux signals into four different quadrants. We present the results associated with this aspect in Sec. III A 3.

3. The quadrant characterization of the flux persistence PDFs

Figure 3 displays the persistence PDFs of $u'w'$ and $w'T'$ signals decomposed into four different quadrants. Additionally, we also compare the persistence PDFs from four quadrants with the total persistence of the heat and momentum signals (see the respective gray circles and inverted triangles in Fig. 3). Such comparison is required to identify at what scales, which quadrant events dominate the persistence behavior of the flux signals.

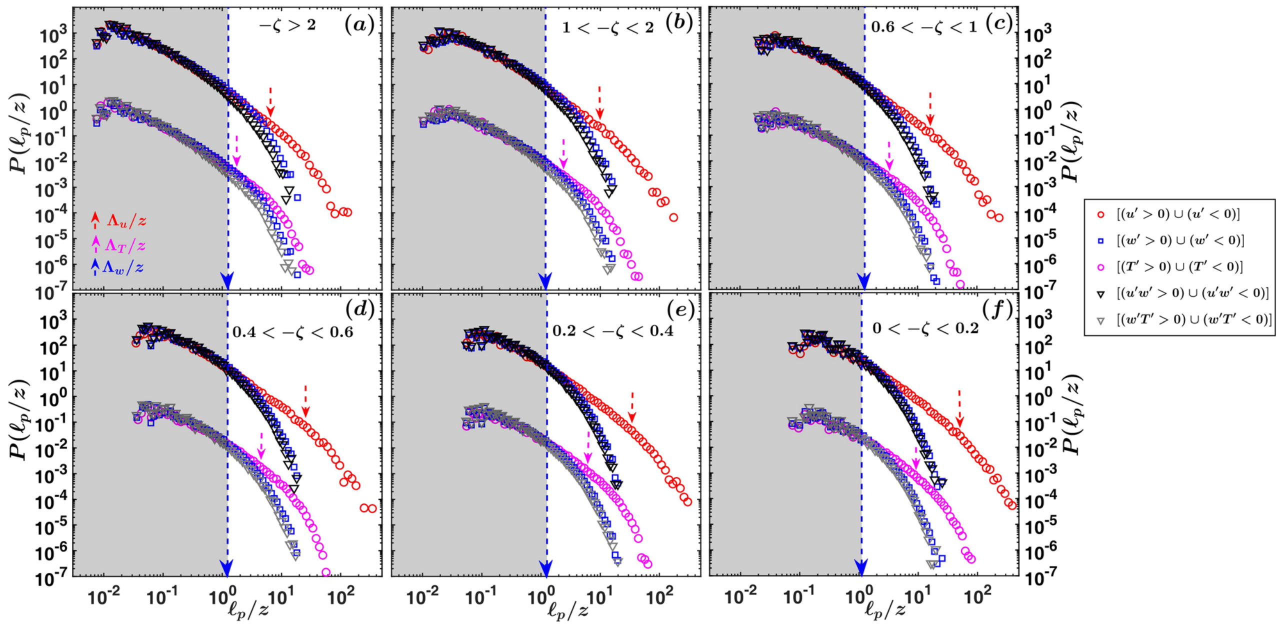

FIG. 2. The persistence PDFs of u' (red circles), T' (pink circles), w' (blue squares), $u'w'$ (black inverted triangles), and $w'T'$ (gray inverted triangles) are shown for the six different stability classes, such as (a) $-\zeta > 2$, (b) $1 < -\zeta < 2$, (c) $0.6 < -\zeta < 1$, (d) $0.4 < -\zeta < 0.6$, (e) $0.2 < -\zeta < 0.4$, and (f) $0 < -\zeta < 0.2$. For visualization purpose, the persistence PDFs of u', w', and $u'w'$ signals are shifted upward by two decades. The colored arrows show the normalized integral length scales of u', T', and w' signals. The regions corresponding to $\ell_p/\Lambda_w \leq 1$ are marked in gray.

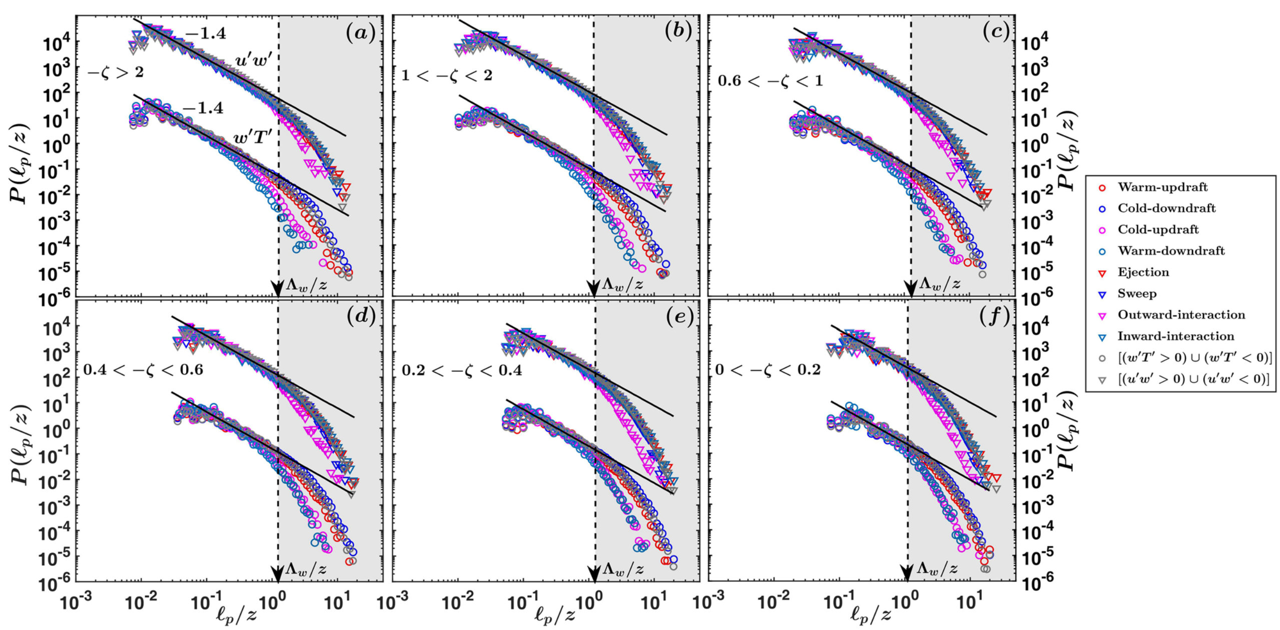

FIG. 3. Same as in Fig. 2 but for $u'w'$ (inverted triangles) and $w'T'$ (circles) signals from the four different quadrants. (a) $-\zeta > 2$, (b) $1 < -\zeta < 2$, (c) $0.6 < -\zeta < 1$, (d) $0.4 < -\zeta < 0.6$, (e) $0.2 < -\zeta < 0.4$, and (f) $0 < -\zeta < 0.2$. For visualization purpose, the persistence PDFs of $u'w'$ signals associated with all the four quadrants are shifted vertically upwards by three decades. The gray inverted triangles and circles denote the $u'w'$ and $w'T'$ persistence PDFs, computed after considering both the positive and negative values together. The regions corresponding to $\ell_p/\Lambda_w > 1$ are marked in gray.

An apparent observation from Fig. 3 is that, for the $u'w'$ signal, the persistence PDFs corresponding to all the four quadrants and their total are in excellent agreement with each other, irrespective of the stability conditions. On the other hand, for the $w'T'$ signal, approximately at scales $\ell_p > \Lambda_w$, the persistence PDFs corresponding to the down-gradient and counter-gradient quadrants remain largely separated from each other. To be precise, for the highly convective stability class ($-\zeta > 2$), the quadrant partition occurs at scales $\ell_p \approx 0.3\Lambda_w$, instead at Λ_w. However, with the decrease in $-\zeta$, the threshold indeed becomes closer to Λ_w. Inspite of such dependency, the threshold at Λ_w serves well to differentiate the transport characteristics between the large and small scale flux events (see Sec. III C). More importantly, the reason behind the quadrant separation for the heat flux events is tied to the fact that the probabilities of encountering long sequences of counter-gradient activities remain significantly low. Interestingly, the discrepancy between the quadrants is quite prominent for the highly convective stability [Fig. 3(a)] but becomes inconspicuous under the near-neutral conditions [Fig. 3(f)].

One also notices that up to the scale $\ell_p \leq \Lambda_w$, the persistence PDFs of the heat and momentum flux signals follow a power-law behavior. Such power-law signatures in the flux persistence PDFs are quite extensive for the highly convective stability [Fig. 3(a)]. Therefore, the data from such stability conditions have been used for the estimation of its exponent. Since we plot the persistence PDFs in log–log plots where the power-law appears as a straight line, the exponent is determined through linear regression for scales $0.01 \leq \ell_p \leq \Lambda_w$. For both the $u'w'$ and $w'T'$ signals, we obtain a best fit exponent of −1.4 with $R^2 > 0.95$. Moreover, to assess the effect of stability on the power-law exponent, the same power-law curves as obtained for the highly convective stability are compared with the other five stability classes [Figs. 3(b)–3(f)]. The comparison shows that, even though there is no discernible change in the slope of the power-law, its extent gradually gets shorter as the ASL approaches the near-neutral stability [Figs. 3(a)–3(f)]. Since the measurements from the near-neutral stability class belong to the lowest three SLTEST levels, the shrinkage in the power-law regime is related to insufficient sampling of the small scale eddies at 20-Hz sampling frequency.[19]

Note that the exponents of this power-law remain same for the $u'w'$ and $w'T'$ signals, being equal to −1.4. This exponent is in excellent agreement with the work of Katul *et al.*,[36] where they found in a convective ASL flow that the persistence time scales of the heat flux events followed a power-law with an exponent of −1.39. However, in that study, they did not consider the momentum flux events or the associated quadrant effects. The analysis of Chowdhuri, Kalmár-Nagy, and Banerjee[19] has revealed that the power-law regimes of the persistence PDFs for the velocity and temperature signals are related to the eddies from the inertial subrange of the turbulence spectrum. Besides, Chowdhuri, Kalmár-Nagy, and Banerjee[19] reported the respective power-law exponents to be equal to −1.6, −1.25, and −1.4 for the u', w', and T' signals. They linked the difference in the exponents to the disparity in the small-scale intermittency, expressed through the framework of self-organized criticality.[46] Interestingly, the power-law exponents corresponding to the flux signals are the same as the T' signal. Further explanation behind this coincidence is elusive at present.

On the other hand, at scales $\ell_p > \Lambda_w$, the deviation from the power-law behavior becomes notable for both the flux persistence PDFs where they follow an exponential distribution, hallmark of a Poisson process.[43] Previous studies have surmised such a phenomenon as a signature of random deformation of the coherent structures due to the presence of the ground.[19,42] For the heat flux ($w'T'$) signals, the quadrant partition only has significance at scales $\ell_p > \Lambda_w$. However, the quadrant segregation does not have any appreciable effect on the persistence PDFs of the momentum flux ($u'w'$) signals at all the scales of motions. Physically, this difference in quadrant behavior between the $u'w'$ and $w'T'$ signals is related to transport asymmetry associated with the down-gradient and counter-gradient quadrants. Such interpretation is feasible, since the contrast between the persistence PDFs of positive and negative values corresponding to any stochastic signal is related to the skewness of that signal, as demonstrated by Chowdhuri, Kalmár-Nagy, and Banerjee.[19] It is worth noting that, in a highly convective ASL, the PDFs of the $w'T'$ signals are significantly asymmetric between the positive and negative values due to the non-Gaussian character of the temperature fluctuations. On the contrary, the PDFs of the $u'w'$ signals are more symmetric because both streamwise and vertical velocity fluctuations are close-to-Gaussian in nature[43] (see Fig. 5 of their work).

From Figs. 2 and 3, one recognizes that the persistence properties of the momentum and heat flux signals exhibit significantly different behavior for scales smaller or larger than the integral scale of the vertical velocity. Since Λ_w is of the same order as z,[19] such discrepancy reflects distinct attributes of turbulent transport associated with the detached and attached eddies, characterized by length scales smaller and larger than z.[47,48] However, it is important to remember that the persistence analysis only provides information on the distribution of time or length scales of the flux events but not on the flux values themselves.[44] Therefore, such analysis alone is insufficient to deduce the effects of the flux events, distinguished by their length scales greater or lesser than Λ_w, on the heat and momentum transport efficiencies. In Sec. III B, we introduce a methodology where the transport characteristics are studied separately for the heat and momentum flux events with length scales $\ell_p > \Lambda_w$ and $\ell_p \leq \Lambda_w$.

B. Polar representation of the quadrant planes

In general, the heat and momentum transport characteristics allied to the turbulent motions are expressed through quadrant analysis, where each point plotted on the u'–w' or T'–w' quadrant plane corresponds to a certain flux event. An example of such a quadrant plot is provided in Fig. S1 (supplementary material) to explain the concepts. The usual practice in this analysis is to report the momentum or heat flux fractions and time fractions from each quadrant and assess the relative importance of the various turbulent motions associated with different flow structures.[10] Additionally, it is also worthwhile to mention that the transport efficiencies of the heat and momentum are intimately linked to the partition of the fluxes among these four different quadrants.[39,40]

On a rudimentary level, the existence of the heat and momentum flux depends upon the strength of the coupling between the two turbulent signals, as described by the governing Navier–Stokes equations. In order to understand the cause of the coupling, it is

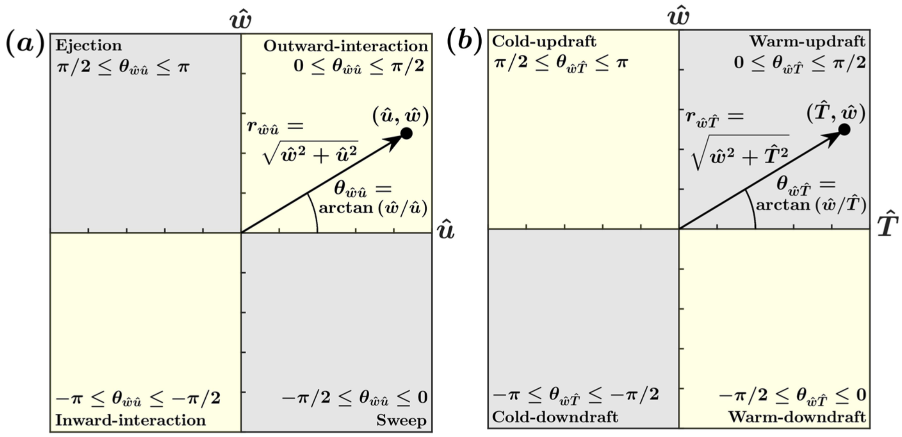

FIG. 4. The graphical illustrations of the (a) u'–w' and (b) T'–w' quadrant planes are provided. The signals u', w', and T' are normalized by their respective standard deviations and denoted as $\hat{u}$, $\hat{w}$, and $\hat{T}$, respectively. In a polar co-ordinate representation, each point on the quadrant plane is described by their amplitudes ($r_{\hat{w}\hat{u}}$ or $r_{\hat{w}\hat{T}}$) and the phase angles ($\theta_{\hat{w}\hat{u}}$ or $\theta_{\hat{w}\hat{T}}$). The gray (yellow) shaded regions in the quadrant planes denote the down (counter)-gradient quadrants.

useful to envisage the quadrant plane as a phase space by drawing analogies with non-linear dynamical systems. From this perspective, each point in the quadrant plane is related to a particular state of flux generation, designated with two parameters that are the phase angles and amplitudes. To accomplish such an objective, the polar representation of the quadrant plane is a well-suited approach.[49]

To explain such an approach, Fig. 4 graphically illustrates the concept of quadrant planes of u'–w' and T'–w' from the perspective of a polar reference frame. Following the standard practice, the u', w', and T' signals in Fig. 4 are normalized by their respective standard deviations (σ_u, σ_w, and σ_T) and denoted as $\hat{x}$ ($\hat{x} = x'/\sigma_x$, where x can be u, w, or T). Such normalization is necessary since it removes the issue regarding the difference in the units while computing the phase angles and amplitudes. In the polar reference frame, each point on the $\hat{x}$–$\hat{w}$ (where x can be u or T) quadrant plane can be associated with an amplitude $r_{\hat{w}\hat{x}}$ and phase angle $\theta_{\hat{w}\hat{x}}$, expressed as

$$\theta_{\hat{w}\hat{x}} = \arctan(\hat{w}/\hat{x}), \tag{17}$$

$$r_{\hat{w}\hat{x}} = \sqrt{\hat{w}^2 + \hat{x}^2}. \tag{18}$$

The lengths of the phase vectors (shown as arrows) on Fig. 4 indicate the values of $r_{\hat{w}\hat{x}}$, whereas $\theta_{\hat{w}\hat{x}}$ are the angles subtended by these vectors with the x axes. The values of the phase angles vary between $-\pi$ and π, and their ranges are related to the four different quadrants, as demonstrated in Table I. For identification purposes, the $\theta_{\hat{w}\hat{x}}$ ranges that denote the down-gradient (counter-gradient) quadrants are marked as gray (yellow) shaded regions in Fig. 4.

In the polar co-ordinate system, the normalized instantaneous flux ($\hat{u}\hat{w}$ or $\hat{w}\hat{T}$) associated with each point is expressed as $(r^2_{\hat{w}\hat{x}} \sin 2\theta_{\hat{w}\hat{x}})/2$. This is because

$$\hat{x}\hat{w} = r_{\hat{w}\hat{x}} \cos(\theta_{\hat{w}\hat{x}}) \times r_{\hat{w}\hat{x}} \sin(\theta_{\hat{w}\hat{x}}) \implies \frac{1}{2} r^2_{\hat{w}\hat{x}} \sin(2\theta_{\hat{w}\hat{x}}), \tag{19}$$

given $\sin(2\theta_{\hat{w}\hat{x}}) = 2\sin(\theta_{\hat{w}\hat{x}})\cos(\theta_{\hat{w}\hat{x}})$ and x can be either u or T.

Subsequently, the averaged normalized flux over all the four quadrants can be written as

$$\overline{\hat{x}\hat{w}} = \frac{1}{2}\overline{r^2_{\hat{w}\hat{x}} \sin 2\theta_{\hat{w}\hat{x}}}. \tag{20}$$

The quantity on the left-hand side of Eq. (20) is the correlation coefficient (R_{wx}), which indicates the transport efficiency of the momentum or the heat fluxes. Apart from that, since $r^2_{\hat{w}\hat{x}}$ is a positive definite quantity, the distribution of the fluxes among the four quadrants is primarily decided by the phase angle $\theta_{\hat{w}\hat{x}}$. Therefore, to simplify the expression in Eq. (20), we may replace the $r^2_{\hat{w}\hat{x}}$ values of every point in the quadrant plane by a single averaged value, $\overline{r^2_{\hat{w}\hat{x}}}$. Note that

$$\overline{r^2_{\hat{w}\hat{x}}} = \overline{\left(\frac{x'}{\sigma_x}\right)^2 + \left(\frac{w'}{\sigma_w}\right)^2} \implies \overline{\left(\frac{x'}{\sigma_x}\right)^2} + \overline{\left(\frac{w'}{\sigma_w}\right)^2}. \tag{21}$$

Since $\overline{(x'/\sigma_x)^2}$ and $\overline{(w'/\sigma_w)^2}$ are both equal to 1, from Eq. (21), it indicates that $\overline{r^2_{\hat{w}\hat{x}}} = 2$. Consequently, this enables us to simplify Eq. (20) as

$$R_{wx} = \frac{\overline{r^2_{\hat{w}\hat{x}}}}{2} \times \overline{\sin 2\theta_{\hat{w}\hat{x}}} \implies \overline{\sin 2\theta_{\hat{w}\hat{x}}} \tag{22}$$

TABLE I. The four quadrants of $\hat{u}$–$\hat{w}$ and $\hat{T}$–$\hat{w}$ and the associated distribution of phase angles in a convective ASL.

Phase angle	$\hat{u}$–$\hat{w}$ quadrant	Quadrant name	$\hat{T}$–$\hat{w}$ quadrant	Quadrant name
$0 \leq \theta_{\hat{w}\hat{u}}, \theta_{\hat{w}\hat{T}} \leq \pi/2$	$\hat{u} > 0, \hat{w} > 0$	Outward-interaction	$\hat{w} > 0, \hat{T} > 0$	Warm-updraft
$\pi/2 \leq \theta_{\hat{w}\hat{u}}, \theta_{\hat{w}\hat{T}} \leq \pi$	$\hat{u} < 0, \hat{w} > 0$	Ejection	$\hat{w} > 0, \hat{T} < 0$	Cold-updraft
$-\pi \leq \theta_{\hat{w}\hat{u}}, \theta_{\hat{w}\hat{T}} \leq -\pi/2$	$\hat{u} < 0, \hat{w} < 0$	Inward-interaction	$\hat{w} < 0, \hat{T} < 0$	Cold-downdraft
$-\pi/2 \leq \theta_{\hat{w}\hat{u}}, \theta_{\hat{w}\hat{T}} \leq 0$	$\hat{u} > 0, \hat{w} < 0$	Sweep	$\hat{w} < 0, \hat{T} > 0$	Warm-downdraft

by substituting $\overline{r^2_{\hat{w}\hat{x}}} = 2$. If the two signals are strictly phase-locked, then the phase angle $\theta_{\hat{w}\hat{x}}$ can take only two values, which are $\pm\pi/4$ and $\pm 3\pi/4$. By replacing those in Eq. (22), one can deduce that the correlation coefficients (R_{wx}) for such occasions would be perfectly ± 1.

To scrutinize this further, from the theory of probability, one can modify Eq. (22) as

$$R_{wx} = \int_{-\pi}^{\pi} P(\theta_{\hat{w}\hat{x}}) \sin(2\theta_{\hat{w}\hat{x}})\, d\theta_{\hat{w}\hat{x}}, \tag{23}$$

where $P(\theta_{\hat{w}\hat{x}})$ is the PDF of the phase angle $\theta_{\hat{w}\hat{x}}$, with the constraint

$$\int_{-\pi}^{\pi} P(\theta_{\hat{w}\hat{x}})\, d\theta_{\hat{w}\hat{x}} = 1. \tag{24}$$

Let us consider another case where the $\theta_{\hat{w}\hat{x}}$ values are uniformly distributed over the quadrant plane such that $P(\theta_{\hat{w}\hat{x}}) = 1/(2\pi)$. This scenario would arise if the phase vectors were oriented in random directions with no phase-locking whatsoever. In that situation, Eq. (23) would be simplified as

$$R_{wx} = \frac{1}{2\pi} \int_{-\pi}^{\pi} \sin(2\theta_{\hat{w}\hat{x}})\, d\theta_{\hat{w}\hat{x}}. \tag{25}$$

Since $\sin(2\theta_{\hat{w}\hat{x}})$ is an odd function, from elemental calculus, we know that the output of the integration in Eq. (25) is 0. This implies a completely inefficient transport of the turbulent fluxes. As a result, the heat and momentum transport efficiency can be judged by investigating the departure of the respective phase angle PDFs from a uniform distribution. An implicit assumption in such argument is that the role played by the amplitudes can be considered to be independent of the phase angles.

The aforementioned method that is based on the polar representation of the quadrant planes offers a unique opportunity to dissect the role of phase coupling toward the transport efficiencies of heat and momentum. It is therefore of practical interest to investigate this aspect corresponding to the flux events with length scales larger or smaller than Λ_w. The intention behind such separation criterion emerges from the flux persistence PDFs, as presented in Figs. 2 and 3. In Fig. 5, we present results to study the distributions of the phase angles and amplitudes in relation to the flux events, conditionally sampled based on the threshold $\ell_p = \Lambda_w$.

Figure 5 shows the PDFs of the phase angles ($\theta_{\hat{w}\hat{x}}$) and amplitudes ($r_{\hat{w}\hat{x}}$) associated with the small and large scale flux events, delineated accordingly with respect to their persistence time scales $\ell_p/\Lambda_w \le 1$ and $\ell_p/\Lambda_w > 1$. Both of these PDFs are computed by collecting all the points that reside within the ensemble of flux events from a particular stability class and persisting for times as prescribed before. Hereafter, we denote these conditional PDFs of the phase

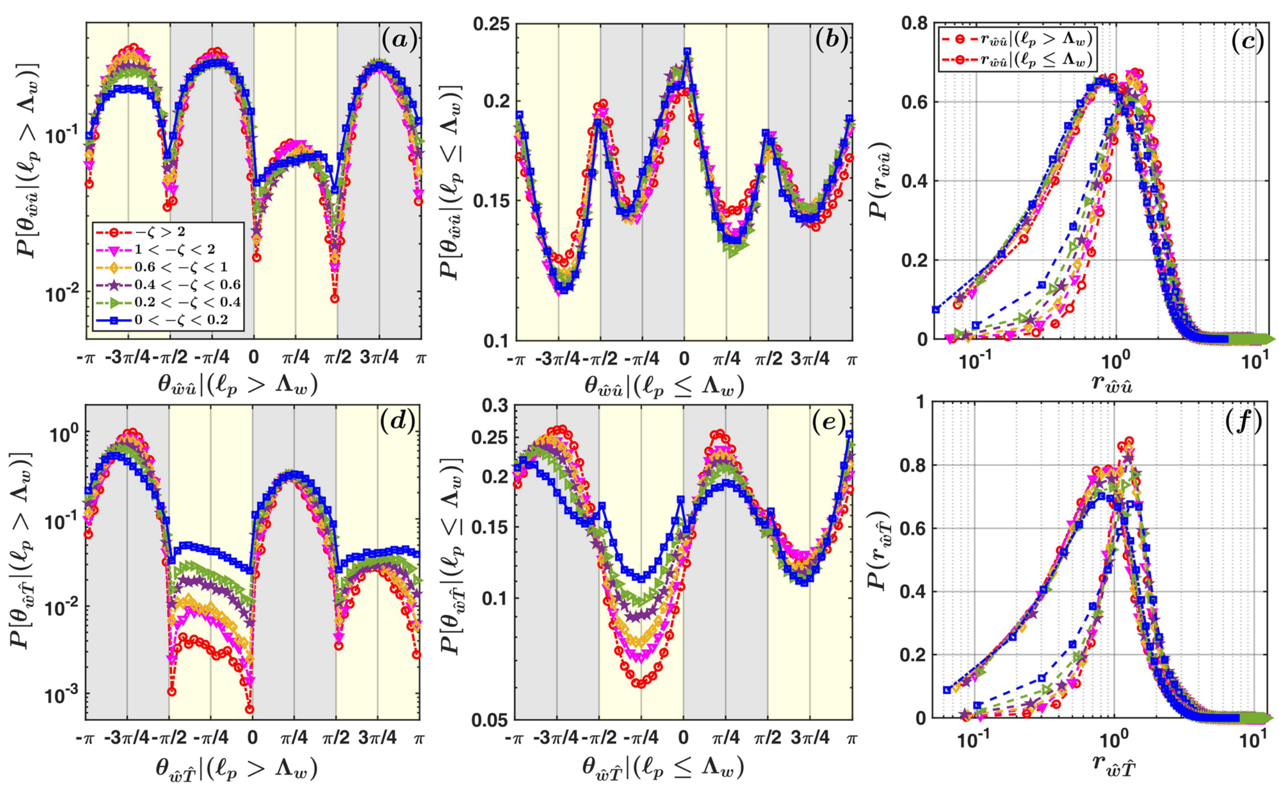

FIG. 5. The PDFs of $\theta_{\hat{w}\hat{u}}$ are shown for the momentum flux events of length scales (a) $\ell_p > \Lambda_w$ or (b) $\ell_p \le \Lambda_w$. Similarly, the PDFs of $\theta_{\hat{w}\hat{T}}$ are shown for the heat flux events corresponding to (d) $\ell_p > \Lambda_w$ and (e) $\ell_p \le \Lambda_w$. The associated PDFs of the amplitudes ($r_{\hat{w}\hat{u}}$ and $r_{\hat{w}\hat{T}}$) are shown in (c) and (f), respectively. The dashed-dotted and the dashed lines in (c) and (f) describe the respective momentum or heat flux events with length scales $\ell_p \le \Lambda_w$ and $\ell_p > \Lambda_w$.

angles as $P[\theta_{\hat{w}\hat{x}}|(\ell_p \le \Lambda_w)]$ and $P[\theta_{\hat{w}\hat{x}}|(\ell_p > \Lambda_w)]$, respectively. Additionally, $P[\theta_{\hat{w}\hat{x}}|(\ell_p \le \Lambda_w)]$ and $P[\theta_{\hat{w}\hat{x}}|(\ell_p > \Lambda_w)]$ individually satisfy the constraint in Eq. (24) so that when integrated over the limit $-\pi$ to π, the result is unity. Other than that, the gray and yellow shaded regions in Figs. 5(a), 5(b), 5(d), and 5(e) identify the ranges of the phase angles that correspond to the regions ascertained to the down-gradient and counter-gradient quadrants, respectively (see Table I and Fig. 4). One may bear in mind that the areas occupied by the phase angle PDFs in these shaded regions are proportional to the fraction of time spent by the signal in that quadrant state. Mathematically, this can be expressed as

$$(T_f)_{\mathrm{X}} = \int_{-\pi}^{\pi} P(\theta_{\hat{w}\hat{x}}) I_{\mathrm{X}}(\theta_{\hat{w}\hat{x}})\, d\theta_{\hat{w}\hat{x}}, \tag{26}$$

where $(T_f)_{\mathrm{X}}$ is time fraction spent in quadrant X (X could be any one of the four quadrants) and $I_{\mathrm{X}}(\theta_{\hat{w}\hat{x}})$ is an identity function that is unity when $\theta_{\hat{w}\hat{x}}$ lies within quadrant X or zero elsewise. In a hypothetical framework, if the two signals are completely phase-locked (phase difference of 0 or π), the PDFs of the phase angles would be a superposition of two Dirac-delta functions at $\theta_{\hat{w}\hat{x}}$ values of $\pm\pi/4$ and $\pm 3\pi/4$. However, for all practical purposes, such a case is not possible since it would imply an infinite persistence of the flux signals as they would never cross the zero. That being said, we thus expect the phase angle PDFs to be distributed in a particular way over all the possible $\theta_{\hat{w}\hat{x}}$.

From Fig. 5(a), the PDFs of the phase angles associated with the large scale momentum flux events display a prominent peak related to the ejection motions (the gray shaded region on the right), irrespective of the stability classes. However, for the negative values of the phase angles, the PDFs have two distinct peaks in the gray and yellow shaded regions with approximately similar values. From Eq. (26), this suggests that for the large scale momentum flux events, there is almost an equal tendency for the phase vectors to either reside within the sweep or within the inward-interaction quadrants. Even so, a minute change in such behavior is observed for the near-neutral stability class. In those conditions, the PDF peak values within the sweep quadrants slightly exceed the values associated with the inward-interaction quadrants.

On the other hand, for all the stability classes, the PDFs of the phase angles associated with the large scale heat flux events exhibit a bi-modal behavior with two distinguished peaks corresponding to the warm-updraft and cold-downdraft motions [the right and left gray shaded regions in Fig. 5(d)]. With the decrease in the thermal stratification, the PDF values of $\theta_{\hat{w}\hat{T}}|(\ell_p > \Lambda_w)$ corresponding to the counter-gradient quadrants [yellow shaded regions in Fig. 5(d)] show a considerable increase.

All these features of the phase angle PDFs associated with the large scale heat and momentum flux events are in sync with the findings of Haugen, Kaimal, and Bradley.[32] They observed that in a convective ASL flow, the heat flux signals mainly exhibited large persistent positive events, whereas for the momentum flux, long sequences of both negative and positive activities were common.

From Fig. 5, one further notices that the shapes of the PDFs of the phase angles differ significantly between the large ($\ell_p > \Lambda_w$) and small ($\ell_p \le \Lambda_w$) scale flux events [Figs. 5(a), 5(b), 5(d), and 5(e)]. For the small scale momentum flux events, an immediate observation is the PDFs of the phase angles is nearly an inverted version of the PDFs associated with the large scale momentum flux events [Fig. 5(b)]. In Fig. 5(b), the maximum values of the PDFs for all the stability classes are located at around 0, with troughs replacing the peaks at approximately the same positions as in Fig. 5(a). Conversely, for the small scale heat flux events [Fig. 5(e)], the behavior of the phase angle PDFs is not completely opposite to that of the large scale events [Fig. 5(d)], but the distinction between the two modes is definitely vague.

In addition to the phase angles, we can also investigate the amplitude PDFs ($r_{\hat{w}\hat{x}}$) for both large and small scale heat and momentum flux events [Figs. 5(c) and 5(f)]. Such information would be important to evaluate whether there are any specific amplitudes that occur most often. From Figs. 5(c) and 5(f), we note that the PDFs of the amplitudes are uni-modal in character, with a shift in their peak positions for the large scale heat or momentum flux events (approximately from 0.8 to 1.2). Apart from that, the PDFs of the amplitudes collapse sufficiently well for all the stability classes, corresponding to the small scale flux events. On the other hand, for the large scale flux events, such collapse is relatively poor for the small values of the amplitudes, located to the left of the peak position.

These results reveal that the statistical characteristics of the phase angles associated with the heat and momentum flux events remain significantly different from each other. Inevitably, this difference is more clearly visible for the flux events with ℓ_p larger than the integral scale of the vertical velocity. To connect the behavior of the phase angle PDFs with the transport efficiencies, from Eq. (20), we can write

$$R_{wx} = \frac{1}{2}\left[\overline{(r^2_{\hat{w}\hat{x}} \sin 2\theta_{\hat{w}\hat{x}})|(\ell_p > \Lambda_w) + (r^2_{\hat{w}\hat{x}} \sin 2\theta_{\hat{w}\hat{x}})|(\ell_p \le \Lambda_w)}\right], \tag{27}$$

where the quantity $(r^2_{\hat{w}\hat{x}} \sin 2\theta_{\hat{w}\hat{x}})$ is divided between the events with scales $\ell_p > \Lambda_w$ and $\ell_p \le \Lambda_w$. From Eq. (23), we can further expand Eq. (27) as

$$\begin{aligned} R_{wx} = \frac{1}{2}\Big[&\langle r^2_{\hat{w}\hat{x}}|(\ell_p > \Lambda_w)\rangle \int_{-\pi}^{\pi} P[\theta_{\hat{w}\hat{x}}|(\ell_p > \Lambda_w)] \\ &\times \sin[2\theta_{\hat{w}\hat{x}}|(\ell_p > \Lambda_w)]\, d\theta_{\hat{w}\hat{x}} + \langle r^2_{\hat{w}\hat{x}}|(\ell_p \le \Lambda_w)\rangle \\ &\times \int_{-\pi}^{\pi} P[\theta_{\hat{w}\hat{x}}|(\ell_p \le \Lambda_w)] \sin[2\theta_{\hat{w}\hat{x}}|(\ell_p \le \Lambda_w)]\, d\theta_{\hat{w}\hat{x}}\Big], \end{aligned} \tag{28}$$

with the constraints

$$\int_{-\pi}^{\pi} P[\theta_{\hat{w}\hat{x}}|(\ell_p > \Lambda_w)]\, d\theta_{\hat{w}\hat{x}} = 1, \tag{29}$$

$$\int_{-\pi}^{\pi} P[\theta_{\hat{w}\hat{x}}|(\ell_p \le \Lambda_w)]\, d\theta_{\hat{w}\hat{x}} = 1, \tag{30}$$

after conditioning the flux events based on their ℓ_p (as shown in Fig. 5). Moreover, in Eq. (28), the angle brackets denote the most probable amplitudes over those events with length scales $\ell_p > \Lambda_w$ and $\ell_p \le \Lambda_w$, respectively. We can replace the most probable amplitudes as 1.2 and 0.8, respectively, obtained from the peak positions of the amplitude PDFs [see Figs. 5(c) and 5(f)].

From the above formulations, it is clear that, in order to evaluate the contribution of the flux events at different length scales to the heat and momentum transport efficiencies, one needs to estimate the departure of $P[\theta_{\hat{w}\hat{x}}|(\ell_p > \Lambda_w)]$ and $P[\theta_{\hat{w}\hat{x}}|(\ell_p \le \Lambda_w)]$ from a uniform distribution. In Sec. III C, we present results to quantify such departure of the phase angle PDFs.

C. Phase angle PDFs and transport efficiency

In order to determine how closely the distribution of the phase angles in Fig. 5 resembles a uniform distribution, it is imperative to consider the cumulative distribution functions (CDFs), instead of the PDFs. This is because the CDFs of a uniform distribution can be represented through a linear function. The CDFs of the phase angles and the equivalent CDFs corresponding to a uniform distribution can be written as

$$F(\theta_{\hat{w}\hat{x}}) = \int_{\pi}^{\theta_{\hat{w}\hat{x}}} P(\theta_{\hat{w}\hat{x}})\, d\theta_{\hat{w}\hat{x}}, \quad (31)$$

$$F_u(\theta_{\hat{w}\hat{x}}) = \frac{\pi - \theta_{\hat{w}\hat{x}}}{2\pi}, \quad (32)$$

where $F(\theta_{\hat{w}\hat{x}})$ is the empirical CDF and $F_u(\theta_{\hat{w}\hat{x}})$ is the CDF for the uniform distribution.

Figure 6 shows the CDFs of the phase angles for the large and small scale heat and momentum flux events and compares those with the CDF of a uniform distribution. An apparent observation from Figs. 6(a) and 6(b) is that irrespective of stability, the statistical characteristics of the CDFs do not seem to differ much from a uniform distribution for both the large and small scale momentum flux events. However, for the large scale heat flux events, the CDFs differ significantly from the uniform distribution [Fig. 6(c)], although such contrast becomes less obvious for the small scale heat flux events [Fig. 6(d)].

Notwithstanding the fact that the CDFs provide a perceptible measure to inspect whether the distributions of the phase angles differ from a uniform distribution, the quantification of such an effect remains an issue. To provide a convenient solution to that, we introduce the normalized Shannon entropy of the phase angle distribution corresponding to the large and small scale flux events. From the information theory,[50–52] the normalized Shannon entropy (H_N) of the phase angle distribution can be defined as

$$H_N(\theta_{\hat{w}\hat{x}}) = -\frac{1}{\ln(N_b)} \sum_{i=1}^{N_b} P_i(\theta_{\hat{w}\hat{x}}) \ln[P_i(\theta_{\hat{w}\hat{x}})], \quad (33)$$

where N_b is the number of bins in which the $\theta_{\hat{w}\hat{x}}$ values are divided (60 in our case) and $P_i(\theta_{\hat{w}\hat{x}})$ is the probability of occurrence of a particular binned value $\theta_{\hat{w}\hat{x}}$. Note that, for a uniform distribution, Eq. (33) will be equal to 1, given that $P_i(\theta_{\hat{w}\hat{x}}) = 1/N_b$ for all the bin indexes. As a consequence, the departure from unity in Eq. (33) is regarded as a metric quantifying the discrepancy with a configuration where the phase vectors are randomly oriented. From Eq. (23), we know that, in the absence of amplitude dependency, this configuration of the phase vectors does not cause any transport of the turbulent fluxes. Therefore, within that constraint, the quantity $H_N(\theta_{\hat{w}\hat{x}})$ can be considered as a proxy for the transport efficiency.

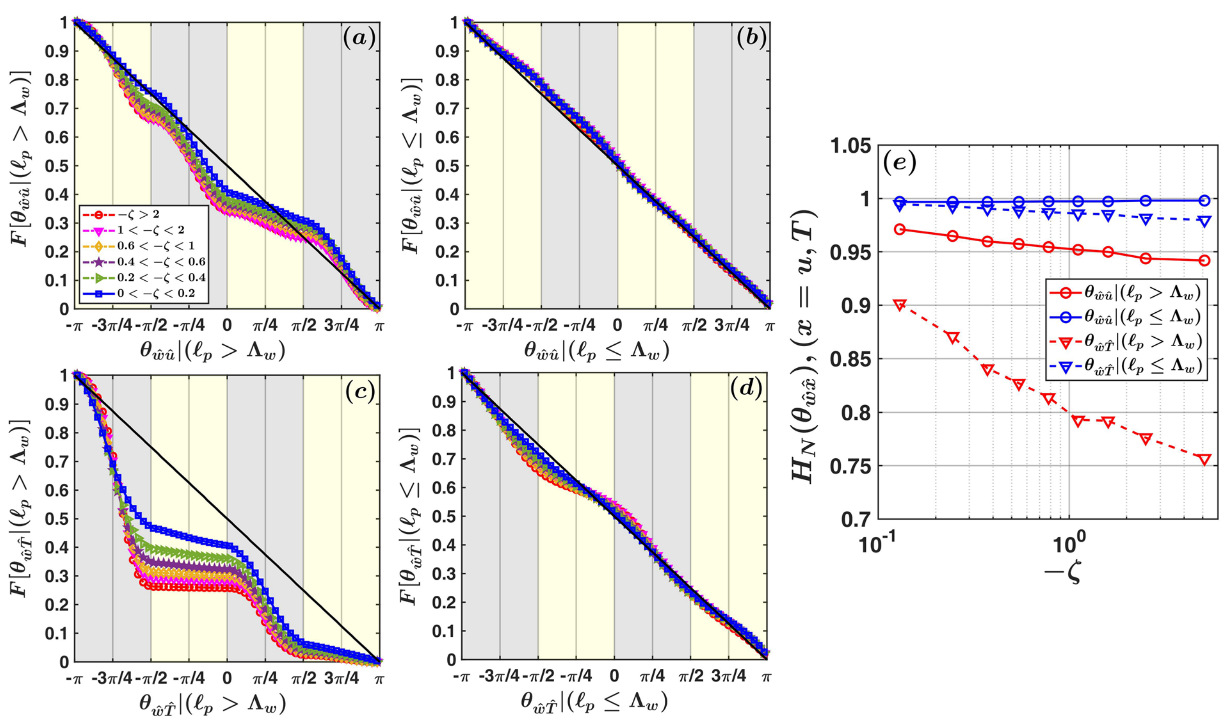

FIG. 6. The CDFs of the phase angles ($\theta_{\hat{w}\hat{u}}$) for the momentum flux events with length scales (a) $\ell_p > \Lambda_w$ and (b) $\ell_p \le \Lambda_w$. Similarly, the CDFs of the phase angles ($\theta_{\hat{w}\hat{T}}$) are shown for the heat flux events corresponding to (c) $\ell_p > \Lambda_w$ and (d) $\ell_p \le \Lambda_w$. The thick black lines denote the CDFs of the uniformly distributed phase angles between $-\pi$ and π. In (e), the normalized Shannon entropy associated with the distribution of the phase angles is shown, corresponding to the length scales $\ell_p > \Lambda_w$ and $\ell_p \le \Lambda_w$.

Figure 6(e) shows the variation of $H_N(\theta_{\hat{w}\hat{x}})$, related to both the small and large scale momentum and heat flux events, with the stability ratio $-\zeta$. Before we discuss the relevant features of Fig. 6(e), it should be noted that the entropies are not computed for single 30-min runs, but for an ensemble of runs within a particular stability bin. This is necessary to ensure that the PDFs of the phase angles are statistically reliable and the estimations of the normalized Shannon entropies are robust. Moreover, in order to document the variation over a substantial range of $-\zeta$ while maintaining the statistical robustness of the results, we divide the $-\zeta$ values into nine number of bins, where each bin contains equal number of 30-min runs (which is 29 for our case, given a total of 261 runs).

From Fig. 6(e), one notices that, for all the stability values, the quantity H_N of the phase angles remains almost equal to unity ($H_N \approx 0.98$), corresponding to both the small scale momentum and heat flux events. Conversely, a considerable departure from unity ($H_N \approx 0.75$) is noted for the large scale heat flux events under highly convective conditions ($-\zeta > 1$). There is also an apparent tendency that the H_N values approach unity ($H_N \approx 0.9$) for the large scale heat flux events as the $-\zeta$ values decrease toward the near-neutral stability. However, for the large scale momentum flux events, no significant departure from unity is noted in its H_N estimates ($H_N \approx 0.96$), irrespective of stability.

To put the above described results into perspective, it is useful to discuss them from the standpoint of turbulent structures and the relation with the heat and momentum transport characteristics in a convective ASL flow. From Fig. 6, it is evident that for the small scale heat and momentum flux events ($\ell_p \leq \Lambda_w$), the phase vectors are oriented in a close-to-random manner with the phase angles being distributed in a quasi-uniform way. From the persistence PDFs of the heat and momentum flux events, we know that at scales $\ell_p \leq \Lambda_w$, the PDF follows a power-law distribution related to the eddies from the inertial subrange (Figs. 2 and 3). According to the Kolmogorov's hypothesis, the turbulence associated with the eddies from the inertial subrange of the spectrum is quasi-isotropic in nature and the eddies hardly transport any heat or momentum.[45,53] Since the random orientation of the phase vectors denotes no flux transport [see Eq. (23)], this complements the properties of turbulence in the inertial subrange, corresponding to scales $\ell_p \leq \Lambda_w$.

On the other hand, for the large scale heat flux events ($\ell_p > \Lambda_w$) associated with the energy containing motions, the distribution of the phase angles differs significantly from the uniform distribution in highly convective stability. This indicates that the vertical velocity and temperature fluctuations are phase-locked to a certain degree in a highly convective ASL flow and hence related to efficient transport of heat [see Eqs. (23) and (28)]. Such a contention is in agreement with the large-eddy simulation studies, where the researchers have shown that both the vertical velocity and temperature patterns overlay on each other in the form of cellular structures.[41,54] This configuration is efficient in transporting the heat flux, which agrees with our assessment. However, the phase angle PDFs between the w' and T' signals gradually resemble a uniform distribution as the near-neutral stability is approached. This behavior is in concurrence with the observation that the heat-transport efficiency decreases as the turbulence becomes more shear dominated.[39] Therefore, we can conclude that the heat-transport efficiency in a convective ASL flow can be explained by the departure of the phase angles from a uniform distribution, corresponding to the events with scales $\ell_p > \Lambda_w$.

Interestingly, an identical deduction cannot be made for the large scale momentum flux events ($\ell_p > \Lambda_w$). This is because, for these events, the phase angle PDFs remain similar to a uniform distribution for all the $-\zeta$ values. From Eq. (28), it would imply that the momentum transport remains inefficient irrespective of the strength of the thermal stratification. However, such an implication does not agree with the ubiquitous result that the momentum transport efficiency increases with the decrease in $-\zeta$. Needless to say, this brings into consideration the role of amplitudes in the momentum flux generation. While connecting the phase angle PDFs directly with the correlation coefficient R_{uw}, it is assumed that the amplitudes of all the phase vectors can be replaced with a single value while preserving their angles. Since such an assumption produces output that is incompatible with the measurements, we thus infer that the amplitude variations play a significant part to generate the momentum flux. Ignoring the amplitude effect results in almost no transport of averaged momentum even during the near-neutral conditions. This agrees with the observations of Haugen, Kaimal, and Bradley,[32] Högström and Bergström,[55] and Narasimha *et al.*[37] where they noted that in a near-neutral ASL flow, the averaged momentum flux is mainly generated through burst like events associated with strong gusts in the streamwise velocity fluctuations. We present our conclusions in Sec. IV.

IV. CONCLUSION

In this study, we provide a detailed account of the persistence properties of turbulent heat and momentum fluxes as obtained from the SLTEST experimental dataset in a convective surface layer. Furthermore, we also establish a novel linkage between the persistence of the flux events and the heat and momentum transport characteristics. We develop such correspondence through a framework based on the concept of phase space in non-linear dynamical systems.

On a larger scale, the ramifications of this research are directed toward providing answers to the questions posed in the Introduction. Keeping that in mind, the important results from this paper are listed as follows:

1. The comparison of the persistence PDFs of momentum and heat fluxes ($u'w'$ and $w'T'$) with the component signals (u' and w' or w' and T') reveals that at scales (ℓ_p) smaller than the integral scale of the vertical velocity (Λ_w), the persistence PDFs of the component signals and their products are in excellent agreement with each other. For such scales, the persistence PDFs of the products ($u'w'$ and $w'T'$) follow an identical power-law distribution with an exponent of −1.4, irrespective of the stability conditions. On the other hand, for scales larger than the integral scale of the vertical velocity, both flux persistence PDFs (of $u'w'$ and $w'T'$) nearly collapse on the persistence PDFs of the w' signals and deviate significantly from the u' or T' signals (see Fig. 2).
2. The flux persistence PDFs are investigated separately by considering the distribution of the time scales from the four different quadrants. We discover that, for the momentum flux events, the persistence PDFs of the $u'w'$ signals are indistinguishable for all the four quadrants by collapsing onto one

another. However, for the heat flux events, the effect of quadrant separation on the $w'T'$ persistence PDFs remains insignificant for scales smaller than the integral scale of the vertical velocity. Contrarily, for $\ell_p > \Lambda_w$, the persistence PDFs of the heat flux events are primarily governed by the down-gradient quadrants, i.e., warm-updrafts and cold-downdrafts.

3. For scales $\ell_p \leq \Lambda_w$, the persistence PDFs of both the flux events show a similar characteristics in terms of quadrant behavior and are also akin to a power-law distribution. Such power-law behavior is related to the eddies from the inertial subrange of the turbulence spectrum. At scales $\ell_p > \Lambda_w$, the persistence PDFs differ from the power-law distribution and drop off exponentially, and the $w'T'$ signals are dominated by the organized heat flux events from the down-gradient quadrants. Therefore, the investigation of flux persistence leads to a criterion that separates two different eddy processes based on the integral scale of w'. Since the integral length scale of w' is of the same order as z, this separation reflects the properties of the attached and detached eddies based on the Townsend's attached eddy model.
4. To gain insight into the transport mechanisms related to these two eddy processes, we scrutinize the phase angles and amplitudes associated with the flux component signals ($\{u', w'\}$ and $\{T', w'\}$). We derive a simple relation between the PDFs of the phase angles and transport efficiencies assuming that the variations in amplitude can be ignored. Under this assumption, the departure of the phase angle PDFs from a uniform distribution is shown to be a necessary condition for flux transport. The results indicate that the phase angles of the component signals related to the heat and momentum flux events with length scales $\ell_p \leq \Lambda_w$ are almost uniformly distributed. Given that these events are associated with the detached eddies from the inertial subrange, this agrees with the general notion that quasi-isotropic turbulence for such size ranges hardly transports any flux.
5. For the large scale heat flux events ($\ell_p > \Lambda_w$), the departure of the phase angle PDFs from a uniform distribution is the strongest for the highly convective regime. However, with the change in stability toward the near-neutral regime, the same PDFs resemble closely a uniform distribution. This variation explains the gradual reduction in the heat transport efficiency as the near-neutral stability is approached.
6. For the large scale momentum flux events, the phase angle PDFs remain close to a uniform distribution irrespective of all the stability classes. This suggests that there is, on average, nearly no transport of momentum in a convective ASL flow. This result is antithetical to the observation that the momentum transport efficiency increases as the ASL approaches the near-neutral conditions. In order to explain the contradiction, the amplitude effects need to be considered for the momentum transport.

In summary, the heat transport efficiency in convective flows is related to the phase angle distributions associated with the events that persist for times larger than the integral scale of vertical velocity. However, for the momentum transport efficiency, the phase information between the streamwise and vertical velocity fluctuations remains largely irrelevant. When amplitude effects are neglected, there is nearly no transport of streamwise momentum. For practical purposes, these results offer a unique perspective toward modeling the heat and momentum transport processes in a convective ASL flow.

SUPPLEMENTARY MATERIAL

See the supplementary material for figures relevant to this article.

AUTHORS' CONTRIBUTIONS

All the authors contributed equally to this work.

ACKNOWLEDGMENTS

Indian Institute of Tropical Meteorology (IITM) is an autonomous institute fully funded by the Ministry of Earth Sciences, Government of India. S.C. and T.P. gratefully acknowledge the Director, IITM, and Dr. Kalmár-Nagy, for the constant encouragement and stimulating discussions during the research. T.B. acknowledges the funding support from the University of California Laboratory Fees Research Program funded by the UC Office of the President (UCOP; Grant ID LFR-20-653572). Additional support was provided by the new faculty start-up grant provided by the Department of Civil and Environmental Engineering and the Henry Samueli School of Engineering, University of California, Irvine. The authors are indebted to Dr. Keith G. McNaughton for kindly providing them the SLTEST dataset for this research and many insightful discussions on turbulent heat and momentum flux behavior in a convective atmospheric surface layer flow. The helpful comments from the anonymous reviewers and the editor are also gratefully acknowledged.

APPENDIX: TA REPRESENTATION OF THE PRODUCTS

In this section, we briefly discuss how the prediction from Eq. (13) compares with the observations. At a first glance, the relationship provided in Eq. (13) may seem counter-intuitive, as one could naively expect the TA representation of the product of the two signals will be equal to the product of the TAs of the individual components. However, expressing the TA representation of the product in such a way will be incorrect since if both signals are negative (individual TA's equal to 0), their product is positive, and hence, the TA representation would be equal to 1. To demonstrate this, in Fig. S2 (supplementary material), we provide a typical example of the original TA approximated time series of $u'w'$ and $w'T'$ for a highly convective stability corresponding to $-\zeta = 10.6$. We compare the original $(u'w')_{\mathrm{TA}}$ and $(w'T')_{\mathrm{TA}}$ with Eq. (13) and with the product $u'_{\mathrm{TA}} \times w'_{\mathrm{TA}}$. The result clearly shows that the expression $u'_{\mathrm{TA}} \times w'_{\mathrm{TA}}$ does not capture the original TA signatures of $(u'w')_{\mathrm{TA}}$ and $(w'T')_{\mathrm{TA}}$, whereas Eq. (13) detains that information perfectly.

DATA AVAILABILITY

The data that support the findings of this study are available from the corresponding author upon reasonable request. The computer codes used in this study are available to all researchers by contacting the corresponding author.

REFERENCES

[1] A. Monin and A. Yaglom, *Statistical Fluid Mechanics: Mechanics of Turbulence* (MIT Press, 1971), Vol. 1.
[2] P. Holmes, J. L. Lumley, G. Berkooz, and C. W. Rowley, *Turbulence, Coherent Structures, Dynamical Systems and Symmetry* (Cambridge University Press, 2012).
[3] S. A. Dixit, A. Gupta, H. Choudhary, A. K. Singh, and T. Prabhakaran, "Asymptotic scaling of drag in flat-plate turbulent boundary layers," Phys. Fluids **32**, 041702 (2020).
[4] D. Baldocchi, E. Falge, L. Gu, R. Olson, D. Hollinger, S. Running, P. Anthoni, C. Bernhofer, K. Davis, R. Evans *et al.*, "FLUXNET: A new tool to study the temporal and spatial variability of ecosystem–scale carbon dioxide, water vapor, and energy flux densities," Bull. Am. Meteorol. Soc. **82**, 2415–2434 (2001).
[5] R. Stöckli, D. Lawrence, G.-Y. Niu, K. Oleson, P. E. Thornton, Z.-L. Yang, G. Bonan, A. Denning, and S. W. Running, "Use of FLUXNET in the community land model development," J. Geophys. Res.: Biogeosci. **113**, G01025, https://doi.org/10.1029/2007jg000562 (2008).
[6] G. I. Taylor, "The spectrum of turbulence," Proc. R. Soc. A **164**, 476–490 (1938).
[7] S. J. Kline, W. C. Reynolds, F. A. Schraub, and P. W. Runstadler, "The structure of turbulent boundary layers," J. Fluid Mech. **30**, 741–773 (1967).
[8] J. M. Wallace, H. Eckelmann, and R. S. Brodkey, "The wall region in turbulent shear flow," J. Fluid Mech. **54**, 39–48 (1972).
[9] S. S. Lu and W. W. Willmarth, "Measurements of the structure of the Reynolds stress in a turbulent boundary layer," J. Fluid Mech. **60**, 481–511 (1973).
[10] J. M. Wallace, "Quadrant analysis in turbulence research: History and evolution," Annu. Rev. Fluid Mech. **48**, 131–158 (2016).
[11] K. N. Rao, R. Narasimha, and M. A. B. Narayanan, "The 'bursting' phenomenon in a turbulent boundary layer," J. Fluid Mech. **48**, 339–352 (1971).
[12] P. H. Alfredsson and A. V. Johansson, "Time scales in turbulent channel flow," Phys. Fluids **27**, 1974–1981 (1984).
[13] T. S. Luchik and W. G. Tiederman, "Timescale and structure of ejections and bursts in turbulent channel flows," J. Fluid Mech. **174**, 529–552 (1987).
[14] R. Narasimha, "The utility and drawbacks of traditional approaches," in *Whither Turbulence? Turbulence at the Crossroads* (Springer, 1990), pp. 13–48.
[15] P. Kailasnath and K. R. Sreenivasan, "Zero crossings of velocity fluctuations in turbulent boundary layers," Phys. Fluids **5**, 2879–2885 (1993).
[16] K. R. Sreenivasan, A. Prabhu, and R. Narasimha, "Zero-crossings in turbulent signals," J. Fluid Mech. **137**, 251–272 (1983).
[17] S. N. Majumdar, "Persistence in nonequilibrium systems," Curr. Sci. **77**, 370–375 (1999).
[18] K. Ghannam, T. Nakai, A. Paschalis, C. A. Oishi, A. Kotani, Y. Igarashi, T. O. Kumagai, and G. G. Katul, "Persistence and memory timescales in root-zone soil moisture dynamics," Water Resour. Res. **52**, 1427–1445, https://doi.org/10.1002/2015wr017983 (2016).
[19] S. Chowdhuri, T. Kalmár-Nagy, and T. Banerjee, "Persistence analysis of velocity and temperature fluctuations in convective surface layer turbulence," Phys. Fluids **32**, 076601 (2020).
[20] A. Townsend, *The Structure of Turbulent Shear Flow* (Cambridge University Press, 1976).
[21] D. O. Mora and M. Obligado, "Estimating the integral length scale on turbulent flows from the zero crossings of the longitudinal velocity fluctuation," Exp. Fluids **61**, 199 (2020).
[22] D. Poggi and G. G. Katul, "Evaluation of the turbulent kinetic energy dissipation rate inside canopies by zero- and level-crossing density methods," Boundary-Layer Meteorol. **136**, 219–233 (2010).
[23] M. Wacławczyk, M. Yong-Feng, J. M. Kopeć, and S. P. Malinowski, "Novel approaches to estimating the turbulent kinetic energy dissipation rate from low- and moderate-resolution velocity fluctuation time series," Atmos. Meas. Tech. **10**, 4573 (2017).
[24] E. O. Akinlabi, M. Wacławczyk, J. P. Mellado, and S. P. Malinowski, "Estimating turbulence kinetic energy dissipation rates in the numerically simulated stratocumulus cloud-top mixing layer: Evaluation of different methods," J. Atmos. Sci. **76**, 1471–1488 (2019).
[25] D. Mora, E. M. Pladellorens, P. R. Turró, M. Lagauzere, and M. Obligado, "Energy cascades in active-grid-generated turbulent flows," Phys. Rev. Fluids **4**, 104601 (2019).
[26] M. Chamecki, "Persistence of velocity fluctuations in non-Gaussian turbulence within and above plant canopies," Phys. Fluids **25**, 115110 (2013).
[27] X. Shang, X. Qiu, P. Tong, and K. Xia, "Measured local heat transport in turbulent Rayleigh-Bénard convection," Phys. Rev. Lett. **90**, 074501 (2003).
[28] Y. Gasteuil, W. Shew, M. Gibert, F. Chilla, B. Castaing, and J. Pinton, "Lagrangian temperature, velocity, and local heat flux measurement in Rayleigh-Bénard convection," Phys. Rev. Lett. **99**, 234302 (2007).
[29] J. Wyngaard, *Turbulence in the Atmosphere* (Cambridge University Press, 2010).
[30] P. A. Davidson, *Turbulence: An Introduction for Scientists and Engineers* (Oxford University Press, 2015).
[31] J. C. Wyngaard, "Atmospheric turbulence," Annu. Rev. Fluid Mech. **24**, 205–234 (1992).
[32] D. A. Haugen, J. C. Kaimal, and E. F. Bradley, "An experimental study of Reynolds stress and heat flux in the atmospheric surface layer," Q. J. R. Meteorol. Soc. **97**, 168–180 (1971).
[33] R. Narasimha and S. V. Kailas, "Turbulent bursts in the atmosphere," Atmos. Environ. **24**, 1635–1645 (1990).
[34] M. R. Duncan and P. H. Schuepp, "A method to delineate extreme structures within airborne flux traces over the FIFE site," J. Geophys. Res.: Atmos. **97**, 18487–18498, https://doi.org/10.1029/91jd03113 (1992).
[35] P. Caramori, P. Schuepp, R. Desjardins, and I. MacPherson, "Structural analysis of airborne flux estimates over a region," J. Clim. **7**, 627–640 (1994).
[36] G. G. Katul, J. Albertson, M. Parlange, C.-R. Chu, and H. Stricker, "Conditional sampling, bursting, and the intermittent structure of sensible heat flux," J. Geophys. Res.: Atmos. **99**, 22869–22876, https://doi.org/10.1029/94jd01679 (1994).
[37] R. Narasimha, S. R. Kumar, A. Prabhu, and S. V. Kailas, "Turbulent flux events in a nearly neutral atmospheric boundary layer," Philos. Trans. R. Soc., A **365**, 841–858 (2007).
[38] H. A. R. De Bruin, W. Kohsiek, and B. J. J. M. Van Den Hurk, "A verification of some methods to determine the fluxes of momentum, sensible heat, and water vapour using standard deviation and structure parameter of scalar meteorological quantities," Boundary-Layer Meteorol. **63**, 231–257 (1993).
[39] D. Li and E. Bou-Zeid, "Coherent structures and the dissimilarity of turbulent transport of momentum and scalars in the unstable atmospheric surface layer," Boundary-Layer Meteorol. **140**, 243–262 (2011).
[40] S. Chowdhuri and T. V. Prabha, "An evaluation of the dissimilarity in heat and momentum transport through quadrant analysis for an unstable atmospheric surface layer flow," Environ. Fluid Mech. **19**, 513–542 (2019).
[41] S. T. Salesky, M. Chamecki, and E. Bou-Zeid, "On the nature of the transition between roll and cellular organization in the convective boundary layer," Boundary-Layer Meteorol. **163**, 41–68 (2017).
[42] D. Cava, G. G. Katul, A. Molini, and C. Elefante, "The role of surface characteristics on intermittency and zero-crossing properties of atmospheric turbulence," J. Geophys. Res.: Atmos. **117**, D01104, https://doi.org/10.1029/2011jd016167 (2012).
[43] S. Chowdhuri, S. Kumar, and T. Banerjee, "Revisiting the role of intermittent heat transport towards Reynolds stress anisotropy in convective turbulence," J. Fluid Mech. **899**, A26 (2020).
[44] A. Bershadskii, J. Niemela, A. Praskovsky, and K. Sreenivasan, "Clusterization and intermittency of temperature fluctuations in turbulent convection," Phys. Rev. E **69**, 056314 (2004).
[45] H. Tennekes and J. Lumley, *A First Course in Turbulence* (MIT Press, 1972).
[46] P. Bak, C. Tang, and K. Wiesenfeld, "Self-organized criticality," Phys. Rev. A **38**, 364 (1988).
[47] I. Marusic and J. P. Monty, "Attached eddy model of wall turbulence," Annu. Rev. Fluid Mech. **51**, 49–74 (2019).
[48] R. Hu, X. I. A. Yang, and X. Zheng, "Wall-attached and wall-detached eddies in wall-bounded turbulent flows," J. Fluid Mech. **885**, A30 (2020).
[49] L. Mahrt and J. Paumier, "Heat transport in the atmospheric boundary layer," J. Atmos. Sci. **41**, 3061–3075 (1984).

[50]C. E. Shannon, "A mathematical theory of communication," Bell Syst. Tech. J. **27**, 379–423 (1948).
[51]T. Banerjee, N. Vercauteren, M. Muste, and D. Yang, "Coherent structures in wind shear induced wave–turbulence–vegetation interaction in water bodies," Agric. For. Meteorol. **255**, 57–67 (2018).
[52]Y. Li, J.-I. Yano, and Y. Lin, "Is atmospheric convection organised?: Information entropy analysis," Geophys. Astrophys. Fluid Dyn. **113**, 553–573 (2019).
[53]J. C. Wyngaard and O. R. Coté, "Cospectral similarity in the atmospheric surface layer," Q. J. R. Meteorol. Soc. **98**, 590–603 (1972).
[54]S. Khanna and J. G. Brasseur, "Three-dimensional buoyancy-and shear-induced local structure of the atmospheric boundary layer," J. Atmos. Sci. **55**, 710–743 (1998).
[55]U. Högström and H. Bergström, "Organized turbulence structures in the near-neutral atmospheric surface layer," J. Atmos. Sci. **53**, 2452–2464 (1996).